A general synthetic method for high-entropy alloy subnanometer ribbons

Lu Tao,[†,#] Mingzi Sun,[‡,#] Yin Zhou,[†] Mingchuan Luo,[†] Fan Lv,[†] Menggang Li,[†] Qinghua Zhang,[§] Lin Gu,[§] Bolong Huang,[‡,*] and Shaojun Guo[†,*]

[†]School of Materials Science and Engineering, Peking University, Beijing, 100871, China.

[‡]Department of Applied Biology and Chemical Technology, The Hong Kong Polytechnic University, Hung Hom, Kowloon, Hong Kong SAR, China.

[§]Beijing National Laboratory for Condensed Matter and Institute of Physics, Chinese Academy of Sciences, Beijing, 100190, China.

[#]These authors contributed equally to this work.

KEYWORDS: high-entropy alloys, two-dimensional, subnanometer ribbons, electrocatalyst, oxygen reduction reaction, Li-O_2 batteries

ABSTRACT: High-entropy alloys (HEAs) are attracting intensive attention due to their broad compositional tunability and interesting catalytic properties. However, precisely shaping the HEAs into suprathin low-dimensional nanostructures for achieving diverse applications remains an enormous challenge owing to their intrinsic thermodynamic instability. Herein we propose a new and general low-temperature method for incorporating up to eight metallic elements into one single-phase subnanometer ribbons to achieve the thinnest HEAs metal materials in the world. We experimentally demonstrate that synthetic processes for suprathin HEAs subnanometer ribbons (SNRs) include: 1) different metal atom nucleation via galvanic exchange reaction between different metal precursors and Ag nanowire template, 2) co-reduction of different metal precursors on nanowire template and 3) the removal of inner Ag core. Density functional theory (DFT) calculations reveal that the crystallization and stabilization of HEAs SNRs strongly depend on the 'highly dynamic' Ag from the template, and the crystallization levels of HEAs subnanometer ribbons are closely correlated with the concentration of Pt and Pd. We demonstrate that the present synthetic method enables the flexible control of components and concentrations in HEAs SNRs for achieving a library of HEAs SNRs and also superior electrocatalytic properties. The well-designed HEA SNRs show great improvement in catalyzing oxygen reduction reaction of fuel cells, and also high discharge capacity, low charge overpotential and excellent durability for Li-O_2 batteries. DFT calculations reveal the superior electrochemical performances are attributed to the strong reduction capability from high-concentration reductive elements in HEAs while the other elements guarantee the site-to-site efficient electron transfer.

INTRODUCTION

Multimetallic nanomaterials have received wide attention due to their extensive applications in electronics, photonics, catalysis and biomedicine.[1-3] Great efforts have been devoted to synthesizing a variety of nanocrystals with well-defined size, composition, shape and structure in the past decades.[4-6] However, the classic alloying strategy was mainly based on two or three compositional elements, albeit turned out to be effective, however, it greatly limits the number of nanoalloys that could be made.[7,8] Recent advances on nanoscale high-entropy alloys (HEAs) that contain four or more elements with similar atomic ratios greatly broaden the alloy design concept and add more compositionally complicated nanoalloys to choose.[9,10] Very recently, breakthrough in the synthesis of HEA nanoparticles and exploring their application in catalysis has been made.[11-14] As far as the catalytic property is concerned, previous studies mainly focus on the regulation of chemical components that can motivate lattice distortion effect and cocktail effect, to optimize the catalytic performance of HEAs.[15,16] Meanwhile, structure engineering, in particular with the regulation of dimensionality and size, has been demonstrated to be an effective way to achieve improved physicochemical properties and unexpected functionalities for nanoalloys, but it is seldom applied in the construction of HEAs.[17-19]

Ultrathin two-dimensional (2D) structure is unique and indispensable configuration for functional materials to access unprecedented chemical, catalytic and electronic properties due to the well-known electron confinement in two dimension that is unattainable neither in other types of nanomaterials nor in their

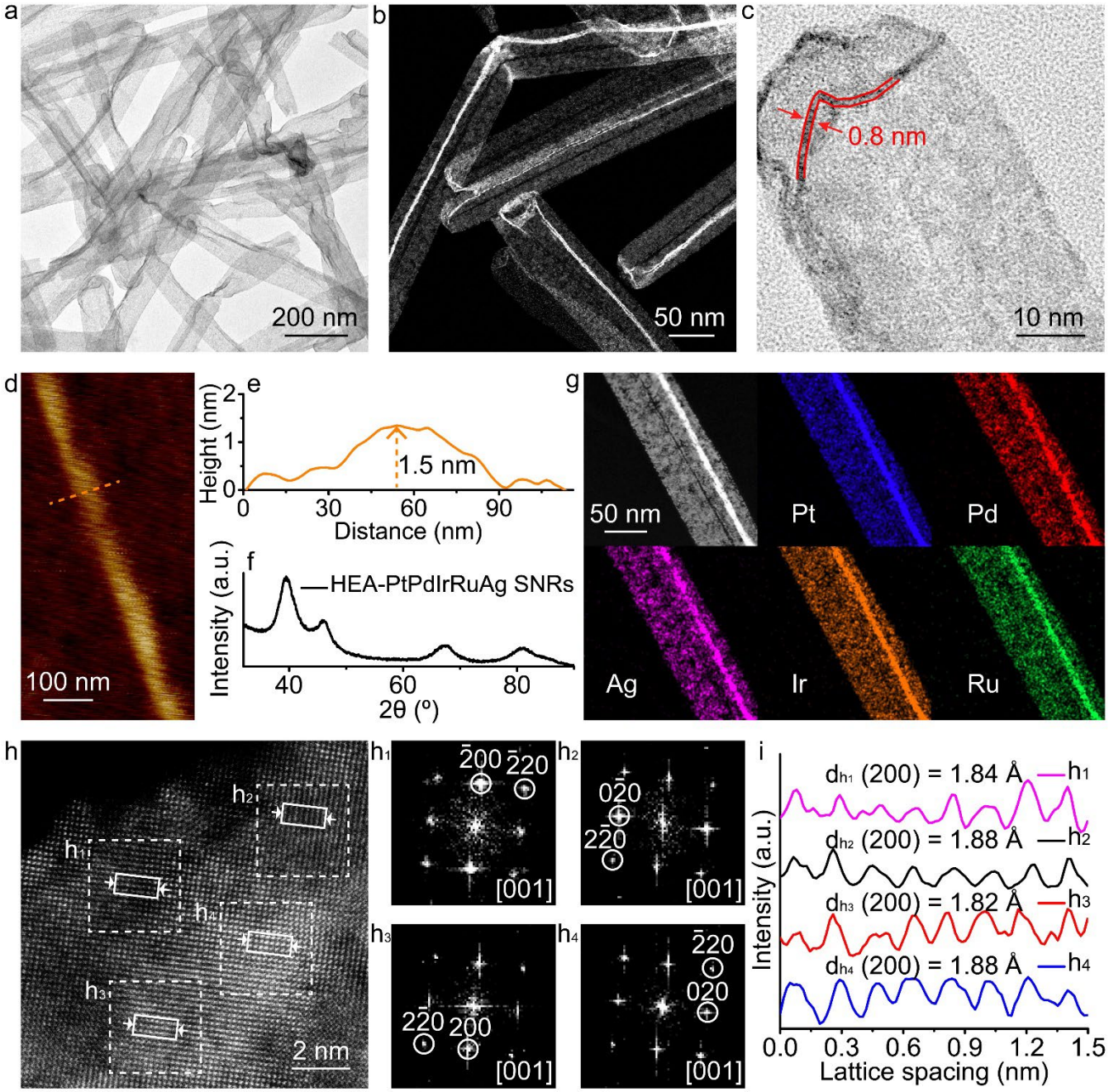

Figure 1. The morphology, composition and structure characterization of HEA-PtPdIrRuAg SNRs. Low-magnification TEM image (a) and HAADF-STEM image (b) of HEA-PtPdIrRuAg SNRs. (c) High-magnification TEM image of one typical HEA-PtPdIrRuAg SNR. AFM image (d) and corresponding height profile (e) of one HEA-PtPdIrRuAg SNR. (f) PXRD pattern of HEA-PtPdIrRuAg SNRs. (g) HAADF-STEM image and EDS element mapping images of one segment of a HEA-PtPdIrRuAg SNR. Pt (blue), Pd (red), Ag (magenta), Ir (orange), and Ru (green) signals. (h) High-resolution HAADF-STEM image of surface atomic arrangement on HEA-PtPdIrRuAg SNR and the corresponding FFT patterns (h_1-h_4) from the dashed white areas in (h). (i) Integrated pixel intensities of HEAs phase were taken from the white solid rectangles in (h).

bulk counterparts.[20-22] What's more, in terms of catalysis, ultrathin 2D architecture features large specific surface areas, abundant active sites and high-density unsaturated atoms, which has been proven to be an ideal alternative structure for designing advanced catalysts in their surface-related applications.[23-25] However, it is still a grand challenge to achieve the 2D anisotropic growth of multicomponent nanocrystals owing to the distinct nucleation/growth kinetics of varied compositional metals in HEAs.[26,27]

Herein, we develop a new and general synthetic method to fabricate suprathin 2D HEAs sub-nanometer ribbons (SNRs) comprised of up to eight metallic elements, especially with a layer thickness of 0.8 nm (the thinnest size of HEAs so far), through the use of Ag nanowires (NWs) as a template. The

time-dependent synthetic mechanism studies reveal that the formation of HEAs SNRs was achieved through unique approaches: 1) different metal atom nucleation via galvanic exchange reaction between different metal precursors with Ag nanowire template, 2) co-reduction of different metal precursors on nanowire template and 3) the removal of inner Ag core. Density functional theory (DFT) calculations reveal that the active Ag and Pd with the largest mean square displacements (MSD) can facilitate the crystallization and stabilization of HEAs-shells on the Ag NWs. As a proof of the catalysis concept, the quinary HEA-PtPdIrRuAg SNRs exhibit a high mass activity of 4.28 A mg_{Pt}^{-1} for oxygen reduction reaction at 0.90 V *versus* reversible hydrogen electrode in alkaline electrolyte, 21.0 times higher than that of commercial Pt/C catalysts. In addition, the senary HEA-PtPdIrRuAuAg SNRs demonstrate impressive performance in Li-O_2 batteries with a low charge overpotential (0.49 V) and an excellent cycle life (100 cycles) under a limited capacity of 1,000 mAh g^{-1} at 0.50 A g^{-1}. DFT calculations were carried out to understand the structural-property correlation of HEAs SNRs through molecule dynamic (MD) simulations and electronic structure interpretations. MD simulations unravel the structural change and atomic arrangements of HEAs SNRs formation, and electronic structures demonstrate the volcano trend of electroactivity and stability based on the balance among metal selections, compositions and the number of elements in HEAs SNRs.

RESULTS AND DISCUSSION

The transmission electron microscopy (TEM) images in Figure 1a and Figure S1 show that the HEA-PtPdIrRuAg SNRs have a width of 50-150 nm and a length of up to several microns. High-angle annular dark-field scanning TEM (HAADF-STEM) image (Figure 1b and Figure S2) show the defect-rich characteristic of the SNRs. The thickness of HEA-PtPdIrRuAg SNR was determined to be about 0.8 nm (Figure 1c), in agreement with the result of atomic force microscopy (AFM) analysis (Figure 1d,e) that the thickness of two overlapped layers is found to be ~1.5 nm. The obtained powder X-ray diffraction (PXRD) pattern (Figure 1f) of HEA-PtPdIrRuAg SNRs exhibits four prominent peaks located at 39.5°, 46.1°, 67.5° and 80.9°, assigned to the (111), (200), (220) and (311) planes of face-centered cubic (*fcc*) crystal phase, respectively, revealing that HEA-PtPdIrRuAg SNRs employ a *fcc* alloy structure without phase segregation. Furthermore, the HAADF-STEM image of one HEA-PtPdIrRuAg SNR and corresponding energy-dispersive X-ray spectroscopy (EDS) elemental mappings (Figure 1g) reveal a homogeneous distribution of Pt, Pd, Ir, Ru and Ag elements in a quinary SNR. The corresponding element ratios are consistent with the ICP result (Figure S3). The atomic resolution HAADF-STEM image (Figure 1h) of surface atomic arrangement on HEA-PtPdIrRuAg SNR and the corresponding fast Fourier transform (FFT) patterns (Figure 1h_1-h_4) further demonstrate that HEA-PtPdIrRuAg SNRs employ a (001)-oriented *fcc* structure. The integrated pixel intensities for the (200) HEAs lattices from various selected areas (Figure 1h) in the HEA-PtPdIrRuAg SNRs are shown in Figure 1i, where the average lattice spacing varies from 1.82 Å (h_3) to 1.84 Å (h_1) and to 1.88 Å (h_2 and h_4), illustrating lattice distortions in the as-obtained quinary HEAs.

The morphological and structural evolution of the 2D HEAs was derived from a kinetically controlled nucleation and growth. In this process, Ag NWs (Figure S4) were firstly mixed with various metal ion precursors (such as Pt^{2+}, Pd^{2+}, *etc*), because of the standard reduction potential of the Ag^+/Ag pair is lower than that of the Pt^{2+}/Pt, Pd^{2+}/Pd, respectively.[28] The outmost Ag on the NWs could be substituted by the above-mentioned precursor metals via a galvanic exchange pathway (such as $Ag+Pd^{2+}\rightarrow 2Ag^{+}+Pd$). This proposed pathway was further certified by means of the measurement of the inductively coupled plasma optical emission spectrometry (ICP-OES), in which the concentration of Ag ions in the solvent increased slightly upon the addition of the mixed precursors metal ions (Table S1). With the addition of precursors solution, the oleylamine (OAm) in the additive solvent enables the co-reduction of the dissolved Ag ion and other additive metal ions on the Ag NWs (Figure S5). By adjusting the quantities of precursors (Table S2), the thickness of the overlayers on the Ag substrates could be tuned from angstroms to nanometers (Figure S6). When subjected to dealloying process, the Ag were found to be etched rapidly by dilute nitric acid so as to generate some local vacancies in the NWs (Figure S6b, at 30 min). Over time, the large-scale dissolution of Ag cores was observed (Figure S7c, d, from 1 h to 3 h). Due to the suprathin thickness, the unbraced shells gradually collapsed into ribbon morphology (Figure S7e-g, from 6 h to12 h). As a result, the dealloying operation gave rise to a new porous 2D HEAs sub-nanostructure (Figure S7h and S8g-i, at 24 h). When the dealloying time was prolonged to another 24 h, there was a negligible change on the morphology (Figure S7i, at 48 h) and composition (Table S1) of the obtained HEAs SNRs. In this design, the controllable nucleation and growth of different compositional metals on the template were realized via galvanic exchange pathway and co-reduction process in the wet-chemical synthesis, and the dealloying strategy achieved the 2D structural evolution of the new HEAs (Figure 2a).

Our synthetic method for HEAs is quite general, and can be used to make senary HEA-PtPdIrRuAuAg SNRs (Figure 2b), septenary HEA-PtPdIrRuAuRhAg SNRs (Figure 2c) and octonary HEA-PtPdIrRuAuRhOsAg SNRs (Figure 2d) with fcc crystal structures (Figure 2e). Remarkably, abundant lattice deformation and defects (such as the part of the red dashed box, Figure 2b) were observed in all of the above-mentioned HEAs SNRs (Figure S9, S10 and S11), mainly generated by the large difference in the sizes of diverse atoms in the HEAs. Besides, serious lattice distortion (red arrow pointed, Figure 2d), as well as disordered lattice (blue arrow pointed, Figure 2d) in the octonary HEA-PtPdIrRuAuRhOsAg SNRs (Figure 2d), could cause more atomic stack faults in one atomic plane, which would bring about obvious Bragg scattering of X-rays on the

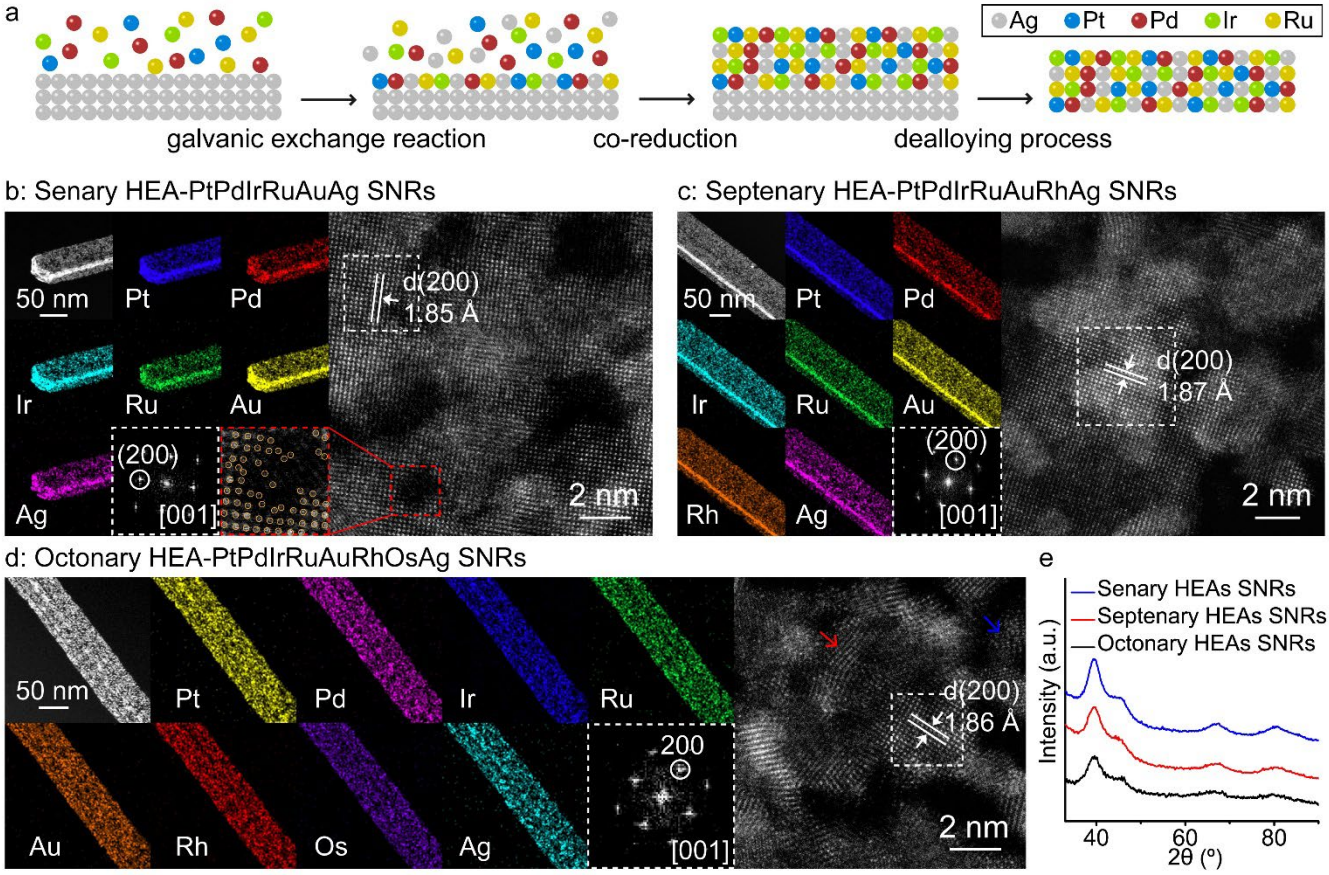

Figure 2. Mechanism and generality for synthesis of HEAs SNRs. (a) Schematic illustration of the proposed galvanic exchange, co-reduction and dealloying pathways in the synthesis of HEAs SNRs. (b) HAADF-STEM image, EDS element mapping images and high-resolution HAADF-STEM image of senary HEA-PtPdIrRuAuAg SNR with the corresponding FFT pattern taken from the white dashed area in (b) and the enlarged atomic-resolution HAADF-STEM image taken from the red dashed square in (b). (c) HAADF-STEM image, EDS element mapping images and high-resolution HAADF-STEM image of septenary HEA-PtPdIrRuAuRhAg SNR with the corresponding FFT pattern taken from the white dashed square in (c). (d) HAADF-STEM image, EDS element mapping images and high-resolution HAADF-STEM image of octonary HEA-PtPdIrRuAuRhOsAg SNR with the corresponding FFT pattern taken from the white dashed square in (d). (e) PXRD patterns of the obtained senary, septenary and octonary HEAs SNRs.

uneven crystal plane, resulting in the weakening and broadening of PXRD diffraction peak intensity of the octonary HEAs SNRs (Figure 2e). The X-ray photoelectron spectroscopy (XPS) results demonstrated that the overall HEA SNRs show metallic states (Figure S12).

To further understand the formation process of HEAs, DFT calculations were carried out through MD simulations. The corresponding DFT models before and after MD simulation are supplied in Figure S13a-d and Figure S13e-h, respectively. For the four different HEAs structures including PtPdIrRuAg, PtPdIrRuAuAg, PtPdIrRuAuRhAg, and PtPdIrRuAuRhOsAg, we probed their structure evolution through the simulated XRD (Figure 3a-d). During the MD process, we notice that all HEAs show the multi peaks pattern with an evident peak at 39.2°, considered as the representative feature of HEAs. The similar XRD characteristic peaks of the structures during MD simulations indicate the overall similar formation process of the HEA SNRs with different compositions. Compared to the perfect Ag crystal structure, the upshifting of peaks at 38.1° and the alleviation of the peak at 44.3° are due to the amorphous structures. After geometry relaxation, we notice the weakening of crystallization based on the weakened peak intensity and increased noise intensity in XRD results. PtPdIrRuAg, PtPdIrRuAuAg, PtPdIrRuAuRhAg and PtPdIrRuAuRhOsAg show the peak at 39.9°, 40.2°, 40.7° and 39.5°, respectively, close to the experimental characterizations (39.5°, 39.7°, 39.8°, and 39.6°, Figure 1f and 2e).

To understand the dynamic of atoms during the formation of HEAs, we compared the mean square displacements (MSD) regarding the elements (Figure 3e-h). Specifically, metal atoms move constantly during the formation of HEAs, and the MSD indicate the position deviation of the metal atoms compared to their original positions over time. As more elements were introduced into the HEAs, the overall MSD also increased, indicating stronger atomic migration behaviors with higher entropy, indicating the potentially increased instability. Notably, Ag and Pd are the most active atoms with the largest MSD during the HEAs formation. Pt shows the median activity during the HEAs formation. In contrast, Ru and Ir are relatively inert atoms, which are possible to induce local aggregation in the HEAs. For

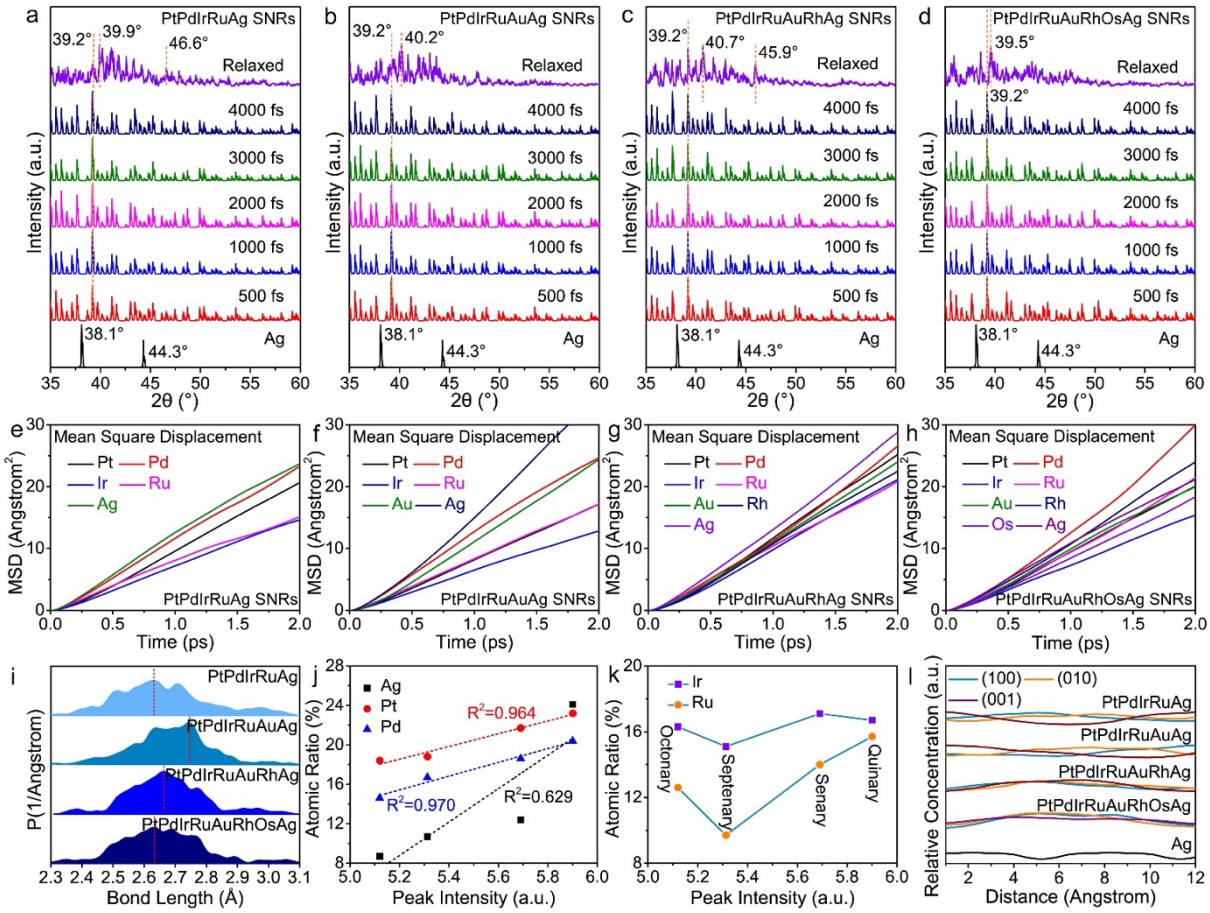

Figure 3. MD simulations of HEAs formation. The XRD evolution for (a) PtPdIrRuAg, (b) PtPdIrRuAuAg, (c) PtPdIrRuAuRhAg and (d) PtPdIrRuAuRhOsAg. The MSD results for (e) PtPdIrRuAg, (f) PtPdIrRuAuAg, (g) PtPdIrRuAuRhAg and (h) PtPdIrRuAuRhOsAg. (i) The bond length distribution in different HEAs. (j) The correlation between Pt, Pd and Ag atomic ratios and the crystallization level obtained by the RDF results. (k) The correlation between Ir and Ru atomic ratios and the crystallization level obtained by the RDF results. (l) The relative concentration in different HEAs from three different directions (100), (010) and (001).

the further introduced elements, Au and Rh are much more dynamic than the Os. These results demonstrate that Ag and Pd are significant factors in facilitating the stabilization and crystallization of HEAs. For the bonding distributions in HEAs, the PtPdIrRuAuAg shows the largest bond length, close to the bond length of the *fcc* structure (Figure 3i). The radial distribution function (RDF) was applied to verify the crystallization level of the HEAs, where the first peak intensity of RDF is strongly correlated with crystallization (Figure 3j). The higher peak intensity represents the higher crystallization levels. The correlation between the intensity of the first peak and the concentration of active metals was demonstrated, in which the atomic ratio of Pd and Pt delivers a linear correlation with the peak intensity with R^2 of 0.970 and 0.964, respectively. Ag shows a weaker correlation with the crystallization, where the R^2 decreases to 0.629. These results further confirm that Pd and Pt are the dominant factors in determining the crystallization level of HEAs. As a comparison, the atomic ratios of inert Ru and Ir show a very weak correlation with the HEAs crystallization level (Figure 3k). The relevant concentration files of the structure from three different directions were also demonstrated (Figure 3l), in which the highly crystallized Ag structure shows the periodic change of constant concentration in different directions while the HEAs structures still show diverse concentrations, indicating the weakened crystallization. These results indicate that Pd and Pt play a significant role in facilitating the crystallization while the other metals cannot evidently affect the formation of HEA SNRs.

The electrocatalytic ORR performance of the quinary HEA-$Pt_{23}Pd_{20}Ir_{17}Ru_{16}Ag_{24}$ SNRs was explored in O_2-saturated 0.1 M KOH, and further compared with commercial Pt/C. We find that the HEA-PtPdIrRuAg SNRs/C had a half-wave potential ($E_{1/2}$) of 0.93 V *versus* reversible hydrogen electrode (RHE) for ORR (Figure 4a), much higher than that of the commercial Pt/C (0.85 V). At 0.90 V, the HEA-PtPdIrRuAg SNRs/C delivered mass activities of 4.28 A mg_{Pt}^{-1} and 1.69 A mg_{PGMs}^{-1} (Pt group metals, PGMs), which is amazingly 21.4 and 8.45 times higher than that of commercial Pt/C (0.20 A mg_{Pt}^{-1}), respectively (Figure 4b). We further tested the electrochemical durability of catalysts by sweeping the potential cycles between 0.6 and 1.1 V in O_2-saturated 0.1 M KOH at 50 mV s^{-1} (Figure 4c and Figure S14). After 10,000 potential cycles, there was almost no change in the half-wave potential of the HEA-PtPdIrRuAg SNRs/C, and the

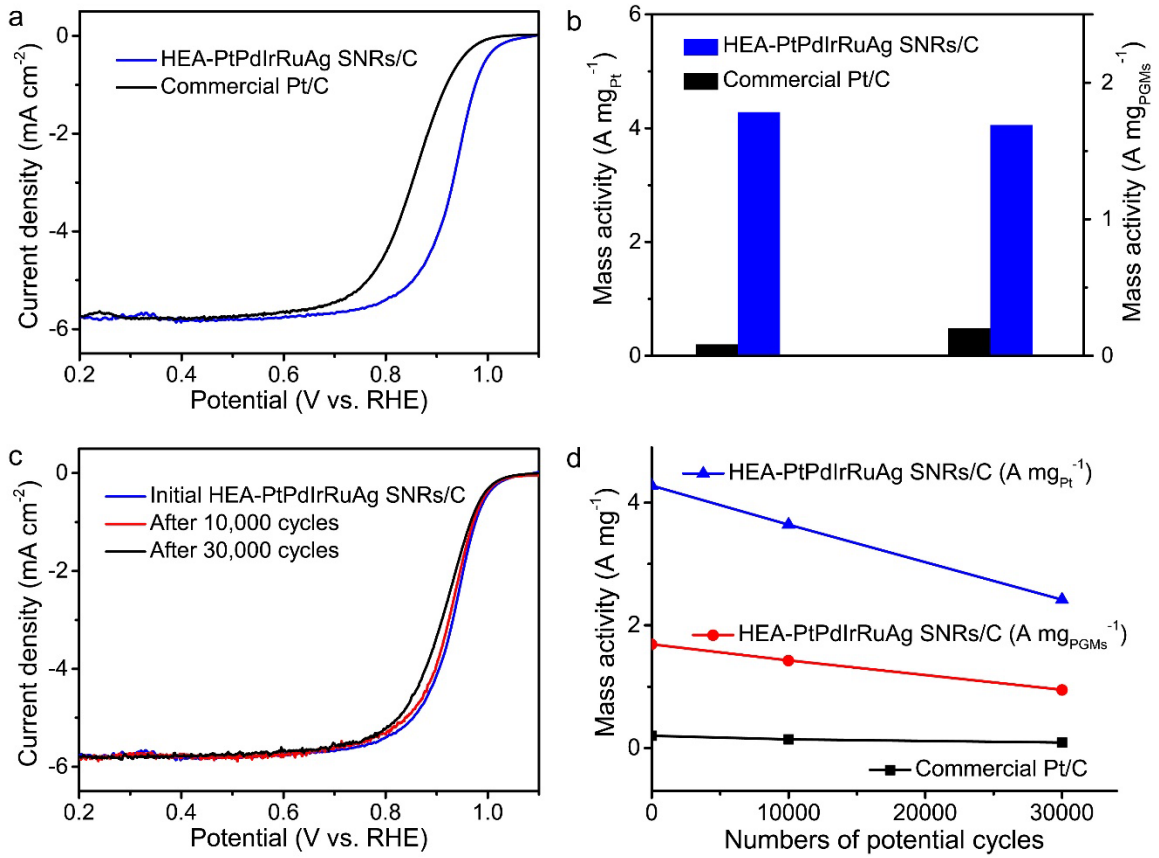

Figure 4. Electrocatalytic performance of HEA-PtPdIrRuAg SNRs/C and commercial Pt/C catalysts for ORR. (a) ORR polarization curves were recorded at room temperature in O_2-saturated 0.1 M KOH aqueous solution at a sweep rate of 20 mV s^{-1} and a rotation rate of 1,600 rpm. (b) Column diagrams of mass activity (normalized with Pt and PGMs, respectively) of different catalysts at 0.9 V *versus* RHE. ORR polarization curves (c) and normalized mass activity changes (d) of the catalysts before and after 10,000 and 30,000 potential cycles between 0.6 V and 1.1 V.

mass activities of HEA-PtPdIrRuAg SNRs/C were maintained at 3.64 A mg_{Pt}^{-1} and 1.43 A mg_{PGMs}^{-1}, 26.0-fold and 10.2-fold higher than those of commercial Pt/C (0.14 A mg_{Pt}^{-1}) over 10,000 potential cycles, respectively (Figure 4d). Over 30,000 potential cycles, the mass activities of HEA-PtPdIrRuAg SNRs/C were still as high as 2.42 A mg_{Pt}^{-1} and 0.95 A mg_{PGMs}^{-1}, and their quinary HEAs phase and porous 2D configuration were well retained (Figure S15). As a comparison, the mass activity of the commercial Pt/C was decreased to be 0.09 A mg_{Pt}^{-1} after 30,000 potential cycles, and the large size changes and substantial aggregation of Pt were observed (Figure S16).

As a proof of demonstration, the $Pt_{22}Pd_{19}Ir_{17}Ru_{14}Au_{16}Ag_{12}$ SNRs/C was explored as a cathode catalyst for Li-O_2 batteries. At 0.10 A g^{-1}, HEA-PtPdIrRuAuAg SNRs/C shows a low charge overpotential of 0.87 V and a high discharge capacity of 5,252 mAh g^{-1} at a current density of 0.10 A g^{-1} (Figure 5a). When the discharge capacity was fixed to 1,000 mAh g^{-1} at 0.10 A g^{-1}, a low charge overpotential of 0.59 V was achieved for HEA-PtPdIrRuAuAg SNRs/C (Figure 5b). With the current density increasing from 0.10 to 1.00 A g^{-1}, the charge overpotential was still below 1.00 V (0.75 V at 1,000 mAh g^{-1}, Figure 5c). The low charge voltage can also be proved by the cyclic voltammetry (CV) curves at 0.05 mV s^{-1} from 2.00 to 4.50 V (Figure 5d), where a low oxidation peak at 0.75 V was visible for HEA-PtPdIrRuAuAg SNRs/C. This result suggests that the HEA-PtPdIrRuAuAg SNRs/C can work as efficient catalysts for Li_2O_2 decomposition. The HEA-PtPdIrRuAuAg SNRs/C based Li-O_2 batteries delivered stable durability for 100 cycles at 0.50 A g^{-1} with a cutoff capacity of 1,000 mAh g^{-1} (Figure 5e). The ex situ X-ray photoelectron spectroscopy (XPS, Figure S17, and S18), scanning electron microscopy (SEM, Figure S19), and XRD patterns (Figure S20) further confirm the excellent reversibility of the HEA-PtPdIrRuAuAg SNRs/C for Li-O_2 batteries.

The electronic structure and electroactivity of HEAs were investigated by DFT calculations. The electronic distributions near the Fermi level (E_F) indicate stronger orbital couplings in the PtPdIrRuAg and PtPdIrRuAuAg than that in the PtPdIrRuAuRhAg and PtPdIrRuAuRhOsAg with more ele-

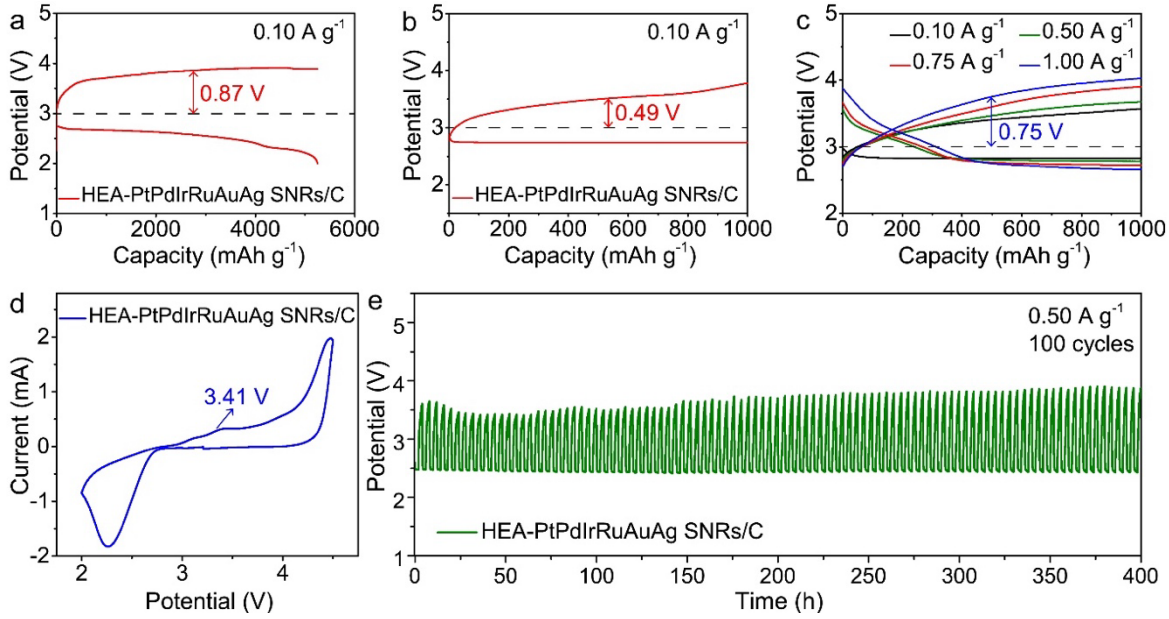

Figure 5. Performance of the Li-O_2 battery. (a) The full discharge-charge curves of HEA-PtPdIrRuAuAg SNRs at 0.10 A g^{-1}. (b) The discharge-charge profiles of HEA-PtPdIrRuAuAg SNRs with the capacity limited to 1,000 mA h g^{-1} at 0.10 A g^{-1}. (c) The rate performance of HEA-PtPdIrRuAuAg SNRs. (d) The CV curves of Li-O_2 batteries with Pt cathodes from 2.00 to 4.00 V at 0.05 mV s^{-1}. (e) The cycle stability of HEA-PtPdIrRuAuAg SNRs at 0.50 A g^{-1} with a limited capacity of 1,000 mAh g^{-1}.

ments (Figure 6a-d). For all the HEAs, most electronic distributions locate near Ru, Ir and Pd, which supply the efficient electron transfer in the HEAs. The projected partial density of states (PDOSs) further reveal the detailed electronic contributions (Figure 6e-h). In PtPdIrRuAg, we notice the evident Pd-4d and Ag-4d peaks at E_V-1.43 eV (E_V=0 eV) and E_V-3.80 eV, respectively. Ir-5d and Ru-4d orbitals show a broad band and cross the E_F, where the high electron density indicates a smaller energy barrier for electron transfer from the HEA surfaces toward the adsorbates, leading to significant improvements in electrocatalysis. The introduction of Au in the PtPdIrRuAuAg further improves the reduction capability with increased electron-rich features (Figure 6f). The involvements of Rh-4d orbitals show strong overlapping with the Ru-4d and Ir-5d orbitals, leading to the weakening of reduction capability (Figure 6g). A similar trend occurs for the PtPdIrRuAuRhOsAg, where the Os-5d bands locate near the E_F, and overlap with the Ru-4d, Ir-5d and Rh-4d, further upshifting the d-band center towards E_F (Figure 6h). Moreover, we also interpret the electronic structures of all the metal pairs in the HEAs. Within PtPdIrRuAg, the Ru-4d and Ir-5d orbitals have shown the broadest coverage, which not only overlaps with d orbitals of other metals but also increases the electron density near the E_F. The improved orbital overlapping improves the site-to-site electron transfer among different metal sites in the HEA SNRs (Figure 6i). When Au is paired with other metals, all the PDOS becomes more electron-rich. In particular, Au-5d orbitals display a good orbital coupling with Ag-4d orbitals, improving the reduction capability of the HEAs (Figure 6j). In contrast, the introduction of Rh and Os both lead to the increased electron density near E_F (Figure 6k-l). In addition, all the PDOS of Os metal pairs shows the evident broadened feature, supporting the enhanced electron transfer efficiency. These electronic structures demonstrate that Pd, Pt, Ag and Au are the key factors in achieving stable HEAs with strong reduction capability. Meanwhile, the Ru, Ir, Rh and Os improve the electron transfer capability. The optimized balance between these two types of metals results in superior performances in ORR and Li-O_2 battery in quinary and senary HEAs. Within the HEAs, the atomic arrangements were studied by the pairing ratios between different elements (Figure 6m). Pt shows high bonding possibility except for Ir and Ru. In particular, Pt and Os are highly preferred at the neighboring sites. As a comparison, due to the strong aggregation trend, other elements show a lower possibility to form bonding with Os. Highly dynamic Ag and Pd show the relatively even possibility to bond with other elements, in which RhAg is the strongly preferred pair. Au only prefers to locate next to the elements with full d orbitals (Pt, Pd, Ag), and the RhAu metal pair shows a low possibility in the HEAs structures.

The ORR and Li-O_2 batteries performances were further investigated by DFT in quinary HEA-PtPdIrRuAg and senary HEA-PtPdIrRuAuAg, respectively. Under the 0 V, the ORR process shows a continuous downhill trend (Figure 6n). The onset potential of 0.93 V was estimated through the reaction energy change, which is consistent with the experimental characterizations (Figure 3a). For the Li-O_2 battery, the discharge process of Li to Li_2O_2 shows a spontaneous conversion (Figure 6o). The discharge and charge potentials were determined to be 2.65 V and 3.42 V, respectively, leading to a 77% of round-trip efficiency. Through DFT calculations, we propose that the selection of elements is significant in determining the property of HEAs (Figure S21). The optimal combinations of reductive (Pt, Pd, Au, and Ag) and oxidative elements (Ru, Ir, Rh, and Os) lead to improved electroactivity. Although more elements lead to more space for HEAs modulations, the increasing number of elements also leads to lower stability due to the local aggregation of specific elements. Therefore, it is significant to find the optimized elements and concentrations to reach remarkable electroactivity towards different electrochemical processes.

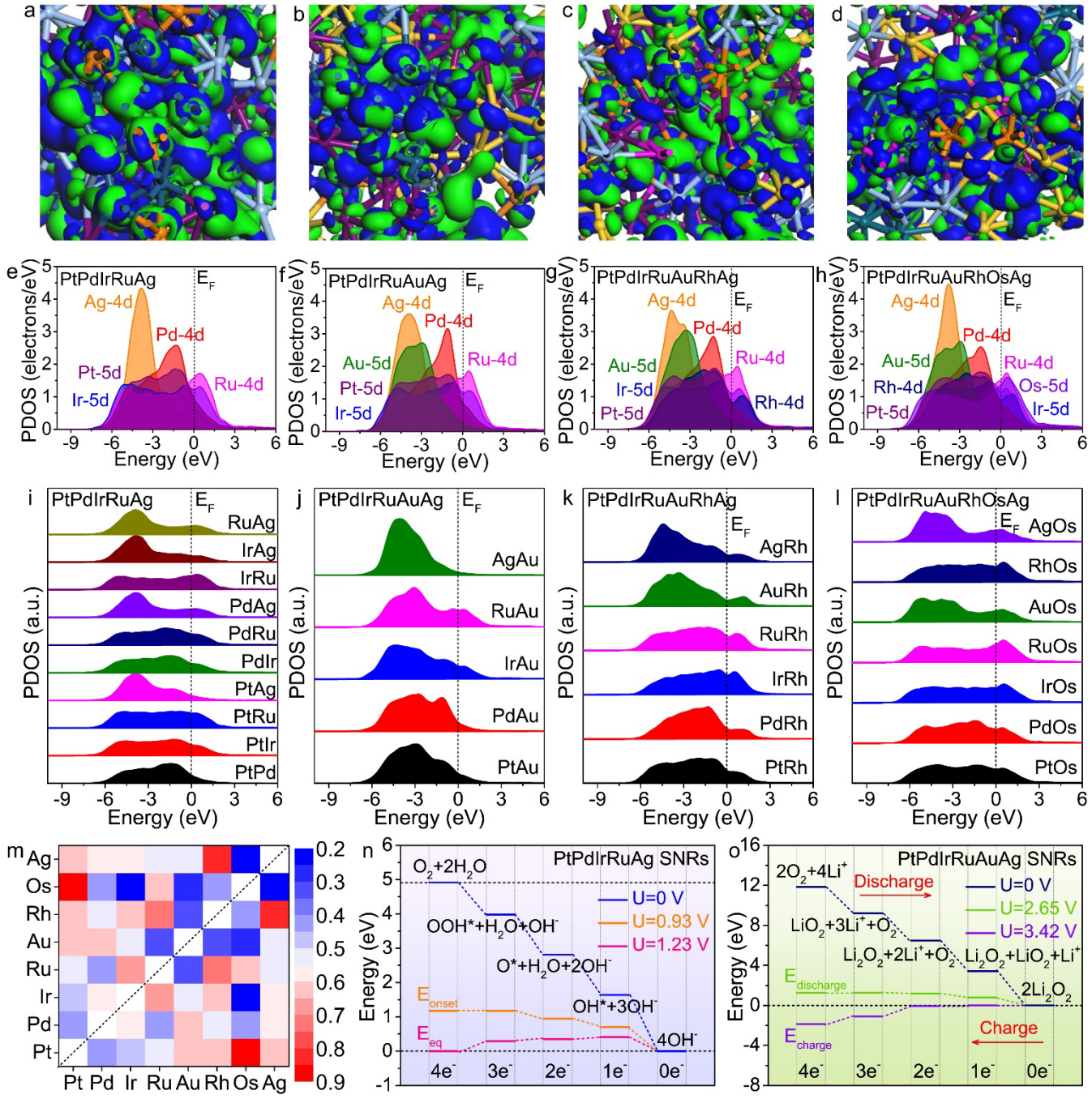

Figure 6. Electronic structures and reaction energy change of HEAs. The 3D contour plot of electronic distributions near EF for (a) PtPdIrRuAg, (b) PtPdIrRuAuAg, (c) PtPdIrRuAuRhAg and (d) PtPdIrRuAuRhOsAg. Pt (dark blue balls), Pd (purple balls), Ir (orange balls), Ru (cyan balls), Rh (pink balls), Au (yellow balls), Os (green balls), and Ag (light blue balls). Blue isosurface indicates bonding orbitals and green isosurface indicates the anti-bonding orbitals near the Fermi level. The PDOS of (e) PtPdIrRuAg, (f) PtPdIrRuAuAg, (g) PtPdIrRuAuRhAg and (h) PtPdIrRuAuRhOsAg. The PDOS evolutions of metal pairs in (i) PtPdIrRuAg, (j) PtPdIrRuAuAg, (k) PtPdIrRuAuRhAg and (l) PtPdIrRuAuRhOsAg. (m) The possibility of atomic pair in different HEAs. The color bar represents the possibility of the bonding between different metals, which ranges from 0 to 1. (n) The ORR performances of quinary PtPdIrRuAg SNRs. (o) The Li-O_2 batteries performances of senary PtPdIrRuAuAg SNRs.

CONCLUSIONS

In conclusion, we report a general synthetic route to construct 2D HEAs SNRs, including but not limited to quinary (PtPdIrRuAg), senary (PtPdIrRuAuAg), septenary (PtPdIrRuAuRhAg), and octonary (PtPdIrRuAuRhOsAg) SNRs. Our synthetic mechanism studies reveal that HEAs SNRs are formed through 1) different metal atom nucleation via the galvanic exchange reaction between different metal precursors with Ag nanowires template, 2) co-reduction of different metal precursors on nanowires template and 3) the removal of

inner Ag core. DFT calculations reveal that the strongest migration of Ag from the template is the fundamental factor in guaranteeing the stabilization of other metal elements in the HEAs. Meanwhile, the concentrations of Pd and Pt are critical to determine the crystallization levels of the HEAs. For catalytic applications, the representative quinary HEA-PtPdIrRuAg SNRs is an efficient and stable electrocatalyst for ORR in alkaline electrolytes, and senary HEA-PtPdIrRuAuAg SNRs show promising performance as a cathode in Li-O_2 batteries. DFT calculations confirm that the concentration of highly dynamic reduction elements (Pd, Pt, Ag, Au) is critical to realize superior electroactivity for HEAs, and the relatively inert oxidative elements (Ir, Ru, Rh, Os) promote the site-to-site electron transfer efficiency but potentially lead to the local aggregations.

ASSOCIATED CONTENT

Supporting Information.
The Supporting Information is available free of charge via the Internet at http://pubs.acs.org.
Methods, Characterization, Electrochemical measurements, Li-O_2 cell assembly and electrochemical measurements, Calculation setup, Figures S1-18, Tables S1, 2 and References (PDF)

AUTHOR INFORMATION

Corresponding Author

Shaojun Guo – School of Materials Science and Engineering, Peking University, Beijing, 100871, China; orcid.org/0000-0003-4427-6837; Email: guosj@pku.edu.cn

Bolong Huang - Department of Applied Biology and Chemical Technology, The Hong Kong Polytechnic University, Hung Hom, Kowloon, Hong Kong SAR, China; orcid.org/0000-0002-2526-2002; Email: bhuang@polyu.edu.hk

Authors

Lu Tao – School of Materials Science and Engineering, Peking University, Beijing, 100871, China

Mingzi Sun - Department of Applied Biology and Chemical Technology, The Hong Kong Polytechnic University, Hung Hom, Kowloon, Hong Kong SAR, China

Yin Zhou – School of Materials Science and Engineering, Peking University, Beijing, 100871, China

Mingchuan Luo – School of Materials Science and Engineering, Peking University, Beijing, 100871, China

Fan Lv – School of Materials Science and Engineering, Peking University, Beijing, 100871, China

Menggang Li – School of Materials Science and Engineering, Peking University, Beijing, 100871, China

Qinghua Zhang – Beijing National Laboratory for Condensed Matter and Institute of Physics, Chinese Academy of Sciences, Beijing, 100190, China

Lin Gu – Beijing National Laboratory for Condensed Matter and Institute of Physics, Chinese Academy of Sciences, Beijing, 100190, China

Complete contact information is available at: https://pubs.acs.org/

Notes

The authors declare no competing financial interest.

ACKNOWLEDGMENT

This work was financially supported by National Key R&D Program of China (2021YFA1501000), the National Science Fund for Distinguished Young Scholars (52025133), the Tencent Foundation through the XPLORER PRIZE, National Natural Science Foundation of China (NSFC) (21771156 and 51671003), the China Postdoctoral Science Foundation (No. 2019M660290), the Natural Science Foundation of China/RGC Joint Research Scheme (N_PolyU502/21), and the funding for Projects of Strategic Importance of The Hong Kong Polytechnic University (Project Code: 1-ZE2V).

REFERENCES

(1) Ferrando, R.; Jellinek, J.; Johnston, R. L. Nanoalloys: from theory to applications of alloy clusters and nanoparticles. *Chem. Soc. Rev.* **2008**, *108*, 846-910.

(2) Grim, J. Q.; Manna, L.; Moreels, I. A sustainable future for photonic colloidal nanocrystals. *Chem. Soc. Rev.* **2005**, *44*, 5897-5914.

(3) Zhou, M.; Li, C.; Fang, J. Noble-metal based random alloy and intermetallic nanocrystals: syntheses and applications. *Chem. Rev.* **2021**, *121*, 736-795.

(4) Xia, Y.; Xiong, Y.; Lim, B.; Skrabalak, S. E. Shape-controlled synthesis of metal nanocrystals: simple chemistry meets complex physics? *Angew. Chem. Int. Ed.* **2009**, *48*, 60-103.

(5) Zherebetskyy, D.; Scheele, M.; Zhang, Y.; Bronstein, N.; Thompson, C.; Britt, D.; Salmeron, M.; Alivisatos, P.; Wang, L.-W. Hydroxylation of the surface of PbS nanocrystals passivated with oleic acid. *Science* **2014**, *344*, 1380-1384.

(6) Weiner, R. G.; Kunz, M. R.; Skrabalak, S. E. Seeding a new kind of garden: synthesis of architecturally defined multimetallic nanostructures by seed-mediated co-reduction. *Acc. Chem. Res.* **2015**, *48*, 2688-2695.

(7) Gilroy, K. D.; Ruditskiy, A.; Peng, H. C.; Qin, D.; Xia, Y. Bimetallic nanocrystals: syntheses, properties, and applications. *Chem. Rev.* **2016**, *116*, 10414-10472.

(8) Koo, W. T.; Millstone, J. E.; Weiss, P. S.; Kim, I. D. The design and science of polyelemental nanoparticles. *ACS Nano* **2020**, *14*, 6407-6413.

(9) Zhang, Y.; Zhou, Y. J.; Lin, J. P.; Chen, G. L.; Liaw, P. K. Solid-solution phase formation rules for multi-component alloys. *Adv. Eng. Mater.* **2008**, *10*, 534-538.

(10) Ye, Y. F.; Wang, Q.; Lu, J.; Liu, C. T.; Yang, Y. Design of high entropy alloys: a single-parameter thermodynamic rule. *Scr. Mater.* **2015**, *104*, 53-55.

(11) Yao, Y.; Huang, Z.; Xie, P.; Lacey, S. D.; Jacob, R. J.; Xie, H.; Chen, F.; Nie, A.; Pu, T.; Rehwoldt, M.; Yu, D.; Zachariah, M. R.; Wang, C.; Shahbazian-Yassar, R.; Li, J.; Hu, L. Carbothermal shock synthesis of high-entropy-alloy nanoparticles. *Science* **2018**, *359*, 1489-1494.

(12) Zhou, Z.; Zhou, Y.; He, Q.; Ding, Z.; Li, F.; Yang, Y. Machine learning guided appraisal and exploration of phase design for high entropy alloys. *npj Comput. Mater.* **2019**, *5*, 128.

(13) Lu, Z.; Chen, Z. W.; Singh, C. V. Neural network-assisted development of high-entropy alloy catalysts: decoupling ligand and coordination effects. *Matter* **2020**, *3*, 1318-1333.

(14) Jiang, B.; Yu, Y.; Cui, J.; Liu, X.; Xie, L.; Liao, J.; Zhang, Q.; Huang, Y.; Ning, S.; Jia, B.; Zhu, B.; Bai, S.; Chen, L.; Pennycook, S. J.; He, J. High-entropy-stabilized chalcogenides with high thermoelectric performance. *Science* **2021**, *371*, 830-834.

(15) Jin, Z.; Lv, J.; Jia, H.; Liu, W.; Li, H.; Chen, Z.; Lin, X.; Xie, G.; Liu, X.; Sun, S.; Qiu, H. J. Nanoporous Al-Ni-Co-Ir-Mo high-entropy alloy for record-high water splitting activity in acidic environments. *Small* **2019**, *15*, e1904180.

(16) Li, S.; Tang, X.; Jia, H.; Li, H.; Xie, G.; Liu, X.; Lin, X.; Qiu, H.-J. Nanoporous high-entropy alloys with low Pt loadings for high-performance electrochemical oxygen reduction. *J. Catal.* **2020**, *383*, 164-171.

(17) Yang, C. C.; Mai, Y.-W. Size, dimensionality, and constituent stoichiometry dependence of physicochemical properties in nanosized binary alloys. *J. Phys. Chem. C* **2013**, *117*, 2421-2426.

(18) Brus, L. Size, dimensionality, and strong electron correlation in nanoscience. *Acc. Chem. Res.* **2014**, *47*, 2951-2959.

(19) Hoye, R. L. Z.; Hidalgo, J.; Jagt, R. A.; Correa-Baena, J. P.; Fix, T.; MacManus-Driscoll, J. L. The role of dimensionality on the optoelectronic properties of oxide and halide perovskites, and their halide derivatives. *Adv. Energy Mater.* **2021**, 2100499.

(20) Novoselov, K. S.; Geim, A. K.; Morozov, S. V.; Jiang, D.; Zhang, Y.; Dubonos, S. V.; Grigorieva, I. V.; Firsov, A. A. Electric field effect in atomically thin carbon films. *Science* **2004**, *306*, 666-669.

(21) Geim, A. K.; Novoselov, K. S. The rise of graphene. *Nat. Mater.* **2007**, *6*, 183-191.

(22) Xu, M.; Liang, T.; Shi, M.; Chen, H. Graphene-like two-dimensional materials. *Chem. Rev.* **2013**, *113*, 3766-3798.

(23) Chen, Y.; Fan, Z.; Zhang, Z.; Niu, W.; Li, C.; Yang, N.; Chen, B.; Zhang, H. Two-dimensional metal nanomaterials: Synthesis, properties, and applications. *Chem. Rev.* **2018**, *118*, 6409-6455.

(24) Luo, M.; Zhao, Z.; Zhang, Y.; Sun, Y.; Xing, Y.; Lv, F.; Yang, Y.; Zhang, X.; Hwang, S.; Qin, Y.; Ma, J. Y.; Lin, F.; Su, D.; Lu, G.; Guo, S. PdMo bimetallene for oxygen reduction catalysis. *Nature* **2019**, *574*, 81-85.

(25) Xing, Y.; Wang, K.; Li, N.; Su, D.; Wong, W.-T.; Huang, B.; Guo, S. Ultrathin RuRh alloy nanosheets enable high-performance lithium-CO_2 battery. *Matter* **2020**, *2*, 1494-1508.

(26) Chen, P.-C.; Liu, M.; Du, J. S.; Meckes, B.; Wang, S.; Lin, H.; Dravid, V. P.; Wolverton, C.; Mirkin, C. A. Interface and heterostructure design in polyelemental nanoparticles. *Science* **2019**, *363*, 959-964.

(27) Xin, Y.; Li, S.; Qian, Y.; Zhu, W.; Yuan, H.; Jiang, P.; Guo, R.; Wang, L. High-entropy alloys as a platform for catalysis: Progress, challenges, and opportunities. *ACS Catal.* **2020**, *10*, 11280-11306.

(28) Bratsch, S. G. Standard electrode potentials and temperature coefficients in water at 298.15 K. *J. Chem. Phys.* **1989**, *18*, 1-21.

A general synthetic method for high-entropy alloy subnanometer ribbons